GDCh

Research Articles

Angewandte
Chemie
International Edition
www.angewandte.org

Supramolecular Rotaxane-Based Multi-Modal Probes for Cancer Biomarker Imaging**

Faustine d'Orchymont and Jason P. Holland

Abstract: Mechanically interlocked molecules present opportunities to construct therapeutic drugs and diagnostic imaging agents but harnessing supramolecular chemistry to make biologically active probes in water is a challenge. Here, we describe a rotaxane-based approach to synthesise radiolabelled proteins and peptides for molecular imaging of cancer biomarkers in vivo. Host–guest chemistry using β-cyclodextrin- and cucurbit-[6]uril-catalysed cooperative capture synthesis produced gallium-68 or zirconium-89 radiolabelled metallo-[4]rotaxanes. Photochemical conjugation to trastuzumab led to a viable positron emission tomography (PET) radiotracer. The rotaxane architecture can be tuned to accommodate different radiometal ion complexes, other protein- or peptide-based drugs, and fluorophores for optical detection. This technology provides a platform to explore how mechanical bonding can improve drug delivery, enhance tumour specificity, control radiotracer pharmacokinetics, and reduce dosimetry.

Introduction

Linking molecules together through non-covalent, mechanical bonds can impart unique physical and chemical features to these supramolecular systems that would be difficult, or even impossible, to achieve through classic synthetic methodology.[1,2] Control over the shape and dynamic motion of mechanically interlocked molecules by using external stimuli has made headlines with the construction of artificial molecular machines.[3–6] Functional[7] supramolecular compounds have also been used in many applications such as logic gates or molecular switches for electronic devices,[8] as molecular nanovalves for controlled

drug release from nanoporous materials,[9] and as catalysts.[10,11]

In a biomedical context, supramolecular coordination complexes show promise in several applications[12,13] from cytotoxic drugs[14–16] and drug delivery vehicles,[17–19] through to biosensors for DNA recognition,[20] and reporter probes for diagnostic molecular imaging.[12] For example, rotaxanes loaded with cytotoxic Pt[14] or Ru[16] complexes, and others capable of selective Ca^{2+} ion binding,[15] have displayed antitumour properties against human cancer cells. Rotaxanes have also been engineered with sophisticated drug-release mechanisms[21,22] that feature enzyme-mediated disassembly and prodrug activation inside tumour cells.[18]

Relatively few examples exist where supramolecular chemistry was employed in the design of molecular imaging agents. Lusby, Archibald and co-workers reported the radiosynthesis of a supramolecular complex by encapsulating the γ-ray emitting $[^{99m}Tc]TcO_4^-$ pertechnetate anion inside the cavity of a tetrahedral $Co^{III}_4L_6$-metallocage, where L is a terpyridine-based ligand (Figure 1a).[23] In vivo imaging showed that the $^{99m}Tc{\supset}$metallocage had a different pharmacokinetic profile compared with free pertechnetate, confirming that the inclusion complex was stable and that the encapsulation strategy is potentially suitable for developing target-specific radiotracers. In a major step toward targeted supramolecular radiotracers, Casini and co-workers demonstrated that the exterior of a $[Pd_2L_4]^{4+}$ metallocage, where L=3,5-*bis*(3-ethynylpyridine)phenyl ligand, can be modified with a blood–brain barrier translocating peptide for potential brain-targeted delivery and non-invasive imaging with the encapsulated $[^{99m}Tc]TcO_4^-$ anion (Figure 1b).[24] Supramolecular techniques have also been used to design fluorescent probes for applications in optical imaging.[25] Smith and co-workers recently used their optically active squaraine dye-rotaxane system[26] to create an interlocked, figure-of-eight molecular knot (Figure 1c).[27] They incorporated cell binding peptide sequences to link the axle termini to a bifunctional macrocycle via Cu^I azide–alkyne click chemistry. The stability and peptide-knot topology, combined with the high brightness of the squaraine dye, shows promise for developing new probes for fluorescence microscopy and biomedical imaging. Hasenknopf and co-workers developed optically active polyrotaxanes for fluorescence imaging,[28] and Gd^{3+}-labelled [3]rotaxanes as highly effective magnetic resonance imaging contrast agents.[29] Supramolecular chemistry has also been utilised in the synthesis of radiolabelled nanoparticles[30] and carbon nanotubes.[31] In spite of their potential, targeted imaging of

[*] Dr. F. d'Orchymont, Prof. Dr. J. P. Holland
University of Zurich, Department of Chemistry
Winterthurerstrasse 190, 8057 Zurich (Switzerland)
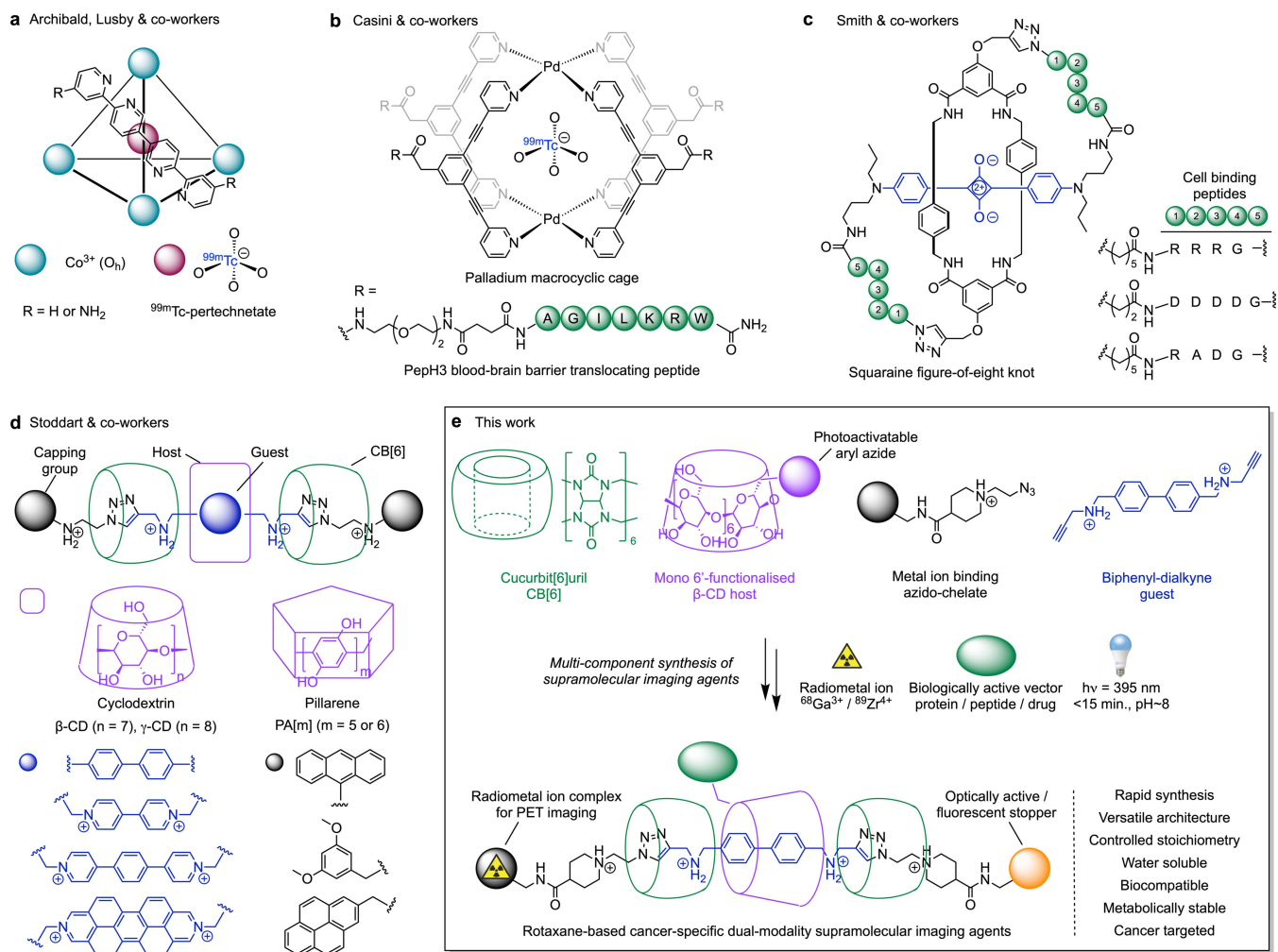E-mail: jason.holland@chem.uzh.ch

Figure 1. Prominent examples of supramolecular complexes developed as molecular imaging agents. a) Tetrahedral Co^{3+}-macrocyclic cages encapsulating $[^{99m}Tc]TcO_4^-$.[23] b) Peptide-functionalised and $[^{99m}Tc]TcO_4^-$ labelled Pd^{2+}-macrocyclic cages featuring blood–brain barrier penetrant translocating sequences.[24] c) Optically active squaraine dye knots for fluorescence imaging of cellular surface markers.[27] d) Cooperative capture synthesis of rotaxanes featuring cucurbit[6]uril, cyclodextrin, and pillar[n]arene macrocycles.[34–36] e) Overview of our approach toward cancer-targeted rotaxanes for PET/optical imaging.

cancer-specific biomarkers with a discrete rotaxane, metallo-cage, or catenane species has remained elusive.

Adapting self-assembly mechanisms to operate in water is a fundamental barrier to using supramolecular chemistry in biological applications.[32] Encouragingly, Bruns et al.[33] reported the near quantitative synthesis of rotaxanes via bioconjugation to peptides and proteins. Here, we report the development of a rotaxane-based approach to create radio-labelled, and optically active, imaging agents that can be conjugated to cancer-targeted monoclonal antibodies or peptide-based drug molecules. Our design strategy employs self-assembly by multiple-component cooperative capture synthesis (Figure 1d).[34–36] The use of a mono-functionalised β-cyclodextrin, with symmetric or unsymmetric axle capping, provides up to three positions for combining radioactive or optically responsive species, with biologically active vectors (Figure 1e). Our long-term goal is to reduce the radiation burden of diagnostic and therapeutic radiotracers by using

supramolecular design principles to control metabolism, distribution, and excretion profiles.
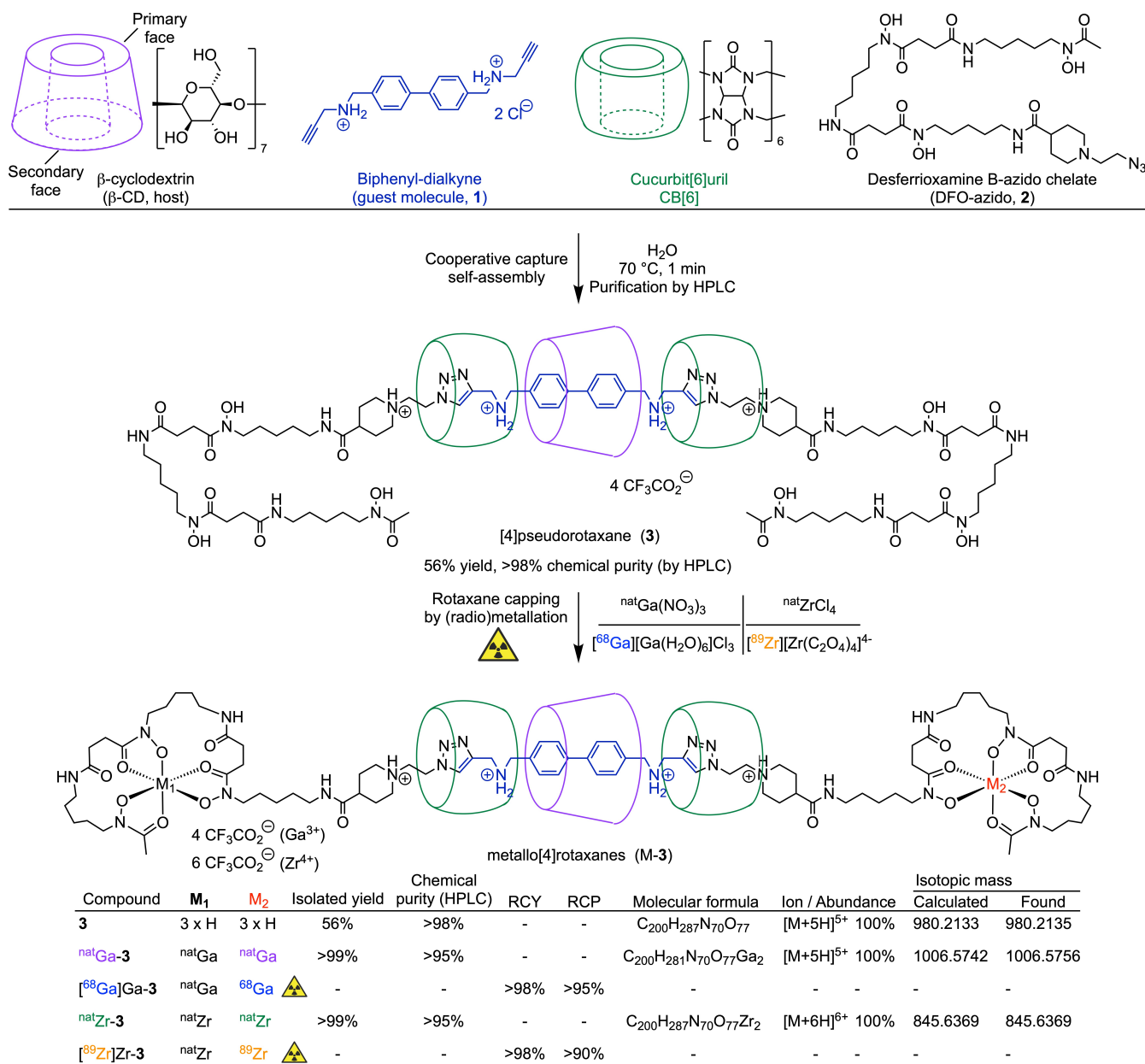
Results and Discussion

In developing our cancer-targeted supramolecular radio-tracers, we first defined the design criteria. The supramolecular methodology should ideally feature rapid self-assembly and generate a molecule with versatile top-ology. The compound should have a well-defined stoichiom-etry that allows for the facile rearrangement or replacement of the different components. The supramolecule should be biocompatible, soluble in water, and stable under the conditions used to label proteins or peptides. For radiotracer synthesis, the probe must be easily purified, and should be chemically and metabolically stable under physiologically relevant conditions. Finally, the imaging probe should display specificity both in vitro and in vivo for the biomarker

of interest and provide lesion-specific accumulation with high image contrast. Taking these points into consideration, cooperative capture synthesis fulfils many of these criteria.[34–36]

In 1983, Mock and Shih[37] reported that 1,3-dipolar cycloaddition reactions between aliphatic azides and terminal alkynes can be accelerated by encapsulation of the reagents inside the macrocyclic cavity of cucurbit[6]uril, CB[6]. The reaction proceeds in accordance with the Pauling principle of catalysis whereby the rate of triazole formation in the presence of CB[6] increased by a factor of 5.5×10^4.[38] CB[6]-promoted click chemistry was later used to make polyrotaxanes,[39] discrete hetero[n]rotaxanes,[34–36] and pro-

tein conjugates.[40] Stoddart and co-workers also discovered that the addition of β- or γ-cyclodextrin (CD), or pillar-[*n*]arene macrocycles to the one-pot, multi-component reaction can increase rates further, due to macrocyclic preorganisation via intermolecular hydrogen-bonding.[36]

Prior to developing a cancer-targeted supramolecular radiotracer, we tested the use of cooperative capture synthesis to make a radiolabelled rotaxane (Scheme 1 and Figure 2; see also Schemes S1–S3, Figure S1–S45 and Table S1 for additional characterisation data). The multi-component reaction involves the addition of one equivalent of biphenyl-dialkyne guest **1** with one equivalent of non-functionalised β-CD to form an initial molecular inclusion

Compound	M_1	M_2	Isolated yield	Chemical purity (HPLC)	RCY	RCP	Molecular formula	Ion / Abundance	Isotopic mass Calculated	Isotopic mass Found
3	3 × H	3 × H	56%	>98%	-	-	$C_{200}H_{287}N_{70}O_{77}$	$[M+5H]^{5+}$ 100%	980.2133	980.2135
natGa-**3**	natGa	natGa	>99%	>95%	-	-	$C_{200}H_{281}N_{70}O_{77}Ga_2$	$[M+5H]^{5+}$ 100%	1006.5742	1006.5756
[68Ga]Ga-**3**	natGa	68Ga ☢	-	-	>98%	>95%	-	- -	-	-
natZr-**3**	natZr	natZr	>99%	>95%	-	-	$C_{200}H_{287}N_{70}O_{77}Zr_2$	$[M+6H]^{6+}$ 100%	845.6369	845.6369
[89Zr]Zr-**3**	natZr	89Zr ☢	-	-	>98%	>90%	-	- -	-	-

Scheme 1. Proof-of-concept synthesis of a radiolabelled rotaxane. Reaction components for the synthesis of the [4]pseudorotaxane **3** and the equivalent metallo[4]rotaxanes labelled with either natural non-radioactive natGa³⁺ or natZr⁴⁺ ions, or the positron-emitting radioactive ions ⁶⁸Ga³⁺ ($t_{1/2} = 67.7$ min.) or ⁸⁹Zr⁴⁺ ($t_{1/2} = 78.41$ h).
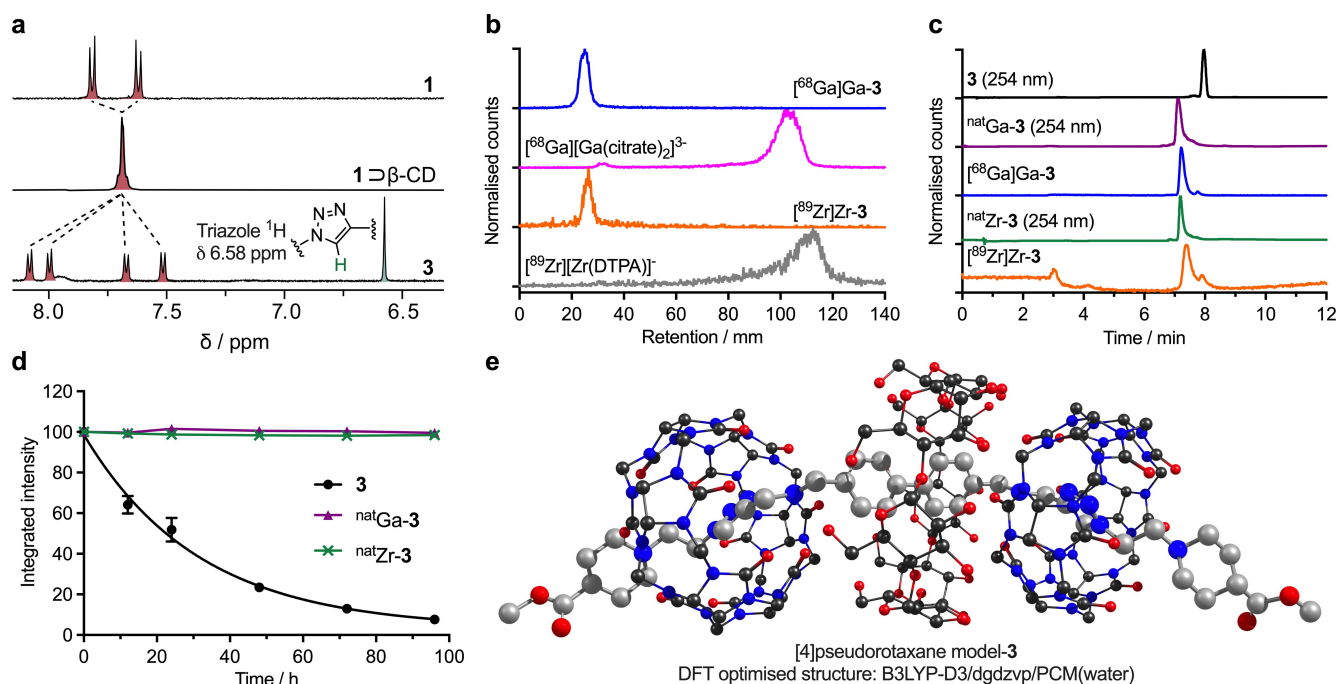
Figure 2. Characterisation of the first radiolabelled rotaxane. a) Selected region of the ^{1}H NMR spectra of **1**, the molecular inclusion complex **1**⊃β-CD, and [4]pseudorotaxane **3** showing the splitting of the biphenyl-alkyne aromatic protons into four distinct environments in the [4]pseudorotaxane. b) Radio-thin-layer chromatography (radio-TLC) chromatograms showing the successful radiosynthesis of metallo[4]rotaxanes [^{68}Ga]Ga-**3** (blue) and [^{89}Zr]Zr-**3** (orange). Controls show the elution of free [^{68}Ga][Ga(citrate)$_2$]$^{3-}$ (pink) and [^{89}Zr][Zr(DTPA)]$^-$ (grey; where DTPA = N,N,N',N'-diethylenetriamine pentaacetic acid) under the radio-TLC conditions. c) Analytical HPLC chromatograms showing the elution profile of **3** (black) and the metallo[4]rotaxanes ^{nat}Ga-**3** (purple), [^{68}Ga]Ga-**3** (blue), ^{nat}Zr-**3** (green), [^{89}Zr]Zr-**3** (orange). Note: non-radioactive samples were monitored by electronic absorption at 254 nm. d) Plot showing the relative stability versus time (measured by HPLC peak integration) of metallo[4]rotaxanes ^{nat}Ga-**3** (purple) and ^{nat}Zr-**3** (green), and the dethreading of [4]pseudorotaxane **3** (black) in water (pH 6–7, 23 °C). e) DFT (B3LYP-D3/dgdzvp/PCM) optimised structure of the model [4]pseudorotaxane showing the axle curvature.

complex (**1**⊃β-CD, Figure 2a, Figure S4–S9). Then, two equivalents of both CB[6] and DFO-azido **2**, a novel derivative of the acyclic metal ion binding chelate desferrioxamine B (DFO) with 1-(2-azidoethyl)piperidine-4-carboxylic acid, are added and the reaction was heated at 70 °C for 1 minute in water. After purification of the crude reaction mixture by using semi-preparative high-performance liquid chromatography (HPLC), [4]pseudorotaxane **3** was isolated in 56 % yield. Compound **3** was characterised by analytical HPLC, electrospray ionisation high-resolution mass spectrometry (HRMS ESI), 1-dimensional and 2-dimensional ^{1}H and ^{13}C{^{1}H} NMR spectroscopy methods (Figure S30–S39). Hydrogen bonding interactions between the CB[6] and β-CD rings restricts the conformational flexibility of the [4]pseudorotaxane **3** with the result that the aromatic proton environments of the encapsulated biphenyl unit become magnetically inequivalent (Figure 2a). Metal ion complexation with ^{nat}Ga(NO$_3$)$_3$ or ^{nat}ZrCl$_4$ (Figure S40–S43) produced the metallo[4]rotaxanes ^{nat}Ga-**3** or ^{nat}Zr-**3** capped at both ends of the axle by the respective ^{nat}Ga^{3+} or ^{nat}Zr^{4+} DFO complexes.

The equivalent radioactive metal ion complexes were synthesised by using stock solutions of [^{68}Ga]GaCl$_3$(aq.) ($t_{1/2}$ = 67.7 min) or [^{89}Zr][Zr(C$_2$O$_4$)$_4$]$^{4-}$(aq.) (also called ^{89}Zr-oxalate, $t_{1/2}$ = 78.41 h). To the best of our knowledge, [^{68}Ga]Ga-**3** and [^{89}Zr]Zr-**3** are the first examples of radio-

labelled rotaxanes. The radioactive products were characterised by analytical radioactive thin-layer chromatography (radio-TLC; Figure 2b) and radio-HPLC (Figure 2c). Both [^{68}Ga]Ga-**3** and [^{89}Zr]Zr-**3** were retained at the baseline (retention factor, R_f = 0.0–0.1), whereas control reactions in the absence of **3** showed the migration of the activity, present as either [^{68}Ga][Ga(citrate)$_2$]$^{3-}$ or [^{89}Zr][Zr-(DTPA)]$^-$, to the solvent front (R_f = 0.9–1.0). Comparison of the radio-HPLC retention times of [^{68}Ga]Ga-**3** or [^{89}Zr]Zr-**3** species with chromatograms of the authenticated non-radioactive samples (measured at 254 nm) confirmed product identities. Both ^{68}Ga- and ^{89}Zr-radiolabelling reactions gave a decay-corrected radiochemical yield (RCY) of > 98 %, and integration of the radio-HPLC chromatograms showed that [^{68}Ga]Ga-**3** and [^{89}Zr]Zr-**3** were obtained with a radiochemical purity (RCP) of > 95 % and > 90 %, respectively.

To develop a targeted supramolecular radiotracer, the mechanical bond must be stable toward disassembly. Stability tests in water confirmed that metallation and axle-capping with either ^{nat}Ga^{3+} or ^{nat}Zr^{4+} ions prevented dethreading of the macrocycles (Figure 2d and Figure S44). The metallo[4]rotaxanes were stable for over 96 h, whereas [4]pseudorotaxane **3** dissociated under the same conditions. Remarkably, HPLC analysis of a lyophilised sample of ^{nat}Ga-**3** after 3-years under ambient conditions (23–30 °C, transparent glass vial) showed no degradation (Figure S45).

Density functional theory (DFT) calculations were also used to optimise the ground-state geometry of a model of [4]pseudorotaxane **3** (Figure 2e). The structure revealed a distinct curvature of the axle which bends to accommodate the three macrocyclic rings. The larger surface area and increased number of hydrogen bond donor groups on the secondary face of β-CD allows for closer contact with CB[6] than on the narrower primary face. This molecular asymmetry, and the increased rigidity of the system, is the origin of splitting observed for the biphenyl protons in the ^{1}H NMR spectrum of **3** (Figure 2a). Compound **3** also displays isomerism due to planar chirality.[2,11]

Next, we synthesised a cancer-targeted rotaxane by installing a photochemically active aryl azide (ArN$_3$) onto the β-CD to create the [4]pseudorotaxane **5**. We then performed the one-pot [89]Zr-radiolabelling and light-induced protein ligation[41,42] to trastuzumab—a monoclonal antibody (mAb) that binds an extracellular epitope of the human epidermal growth-factor receptor 2 (HER2/*neu*).[43,44] Details on the synthesis, radiochemistry and characterisation of [[89]Zr]ZrFe-[4]rotaxane-trastuzumab, [[89]Zr]ZrFe-**6**, are presented in Scheme 2 and Figure 3 (see also Scheme S4, Figure S46–S89 and Tables S2–S4).

In a 6-step procedure, β-CD was mono-functionalised at one of the hydroxyl positions on the primary face to give the photoactivatable derivative β-CD-ArN$_3$ (**4**; Scheme S4 and Figure S46–S62). Cooperative capture synthesis gave [4]pseudorotaxane **5** in 54% yield after purification, which was characterised by HPLC, HRMS, and multinuclear NMR spectroscopy (Figure S63–S69). Metallation of **5** with [nat]Ga[3+] gave metallo[4]rotaxane [nat]Ga-**5**, which was characterised and found to be stable in water for over 96 h (Figure S70–

S72). When **5** or [nat]Ga-**5** was irradiated with a light-emitting diode (LED, 395 nm), rapid photochemical degradation was observed by analytical HPLC (Figure 3a, black curve, and Figure S73). As a control, [nat]Ga-**3** which contains non-functionalised β-CD, was stable toward irradiation (Figure 3a, purple curve). Interestingly, metallation of **5** with [nat]Zr[4+] ions produced the desired metallo[5]rotaxane, [nat]Zr-**5**, where at least three isomers (confirmed by HRMS) with distinct retention times were observed in the analytical HPLC chromatogram (Figure S75–S79). Complexation of Zr[4+] ions by DFO results in multiple geometric and stereochemical isomers in which solvent coordination can also expand coordination numbers from 6 to 8.[47] Planar chirality[2,11] of the rotaxane increases further the number of possible isomers which accounts for the observed profile in the analytical HPLC chromatogram of [nat]Zr-**5**.

Starting from an initial 2:1 mole ratio of [4]pseudorotaxane **5** to mAb, [89]Zr-radiolabelling of **5** and light-induced conjugation to trastuzumab, followed by reaction quenching with FeCl$_3$ and DTPA in situ gave the rotaxane-mAb conjugate, [[89]Zr]ZrFe-**6**. Aliquots of the crude reaction were retained for analysis and [[89]Zr]ZrFe-**6** was purified by manual size-exclusion chromatography (SEC) by using Sephadex G-100 gel filtration columns. The [[89]Zr]ZrFe-**6** product was isolated in sterile PBS (pH 7.4) with a decay-corrected RCY of $14.0 \pm 5.0\%$ ($n=3$), an average RCP of $91 \pm 2\%$ (measured by radio-SEC-HPLC), and a molar activity A_m of 0.604–0.671 MBq nmol^{−1} of protein. [[89]Zr]ZrFe-**6** was characterised by radio-TLC and analytical size-exclusion chromatography (SEC) coupled to a HPLC (Figures 3b and c, and Figure S80, S81). Radio-TLC analysis confirmed that quantitative radiochemical conver-
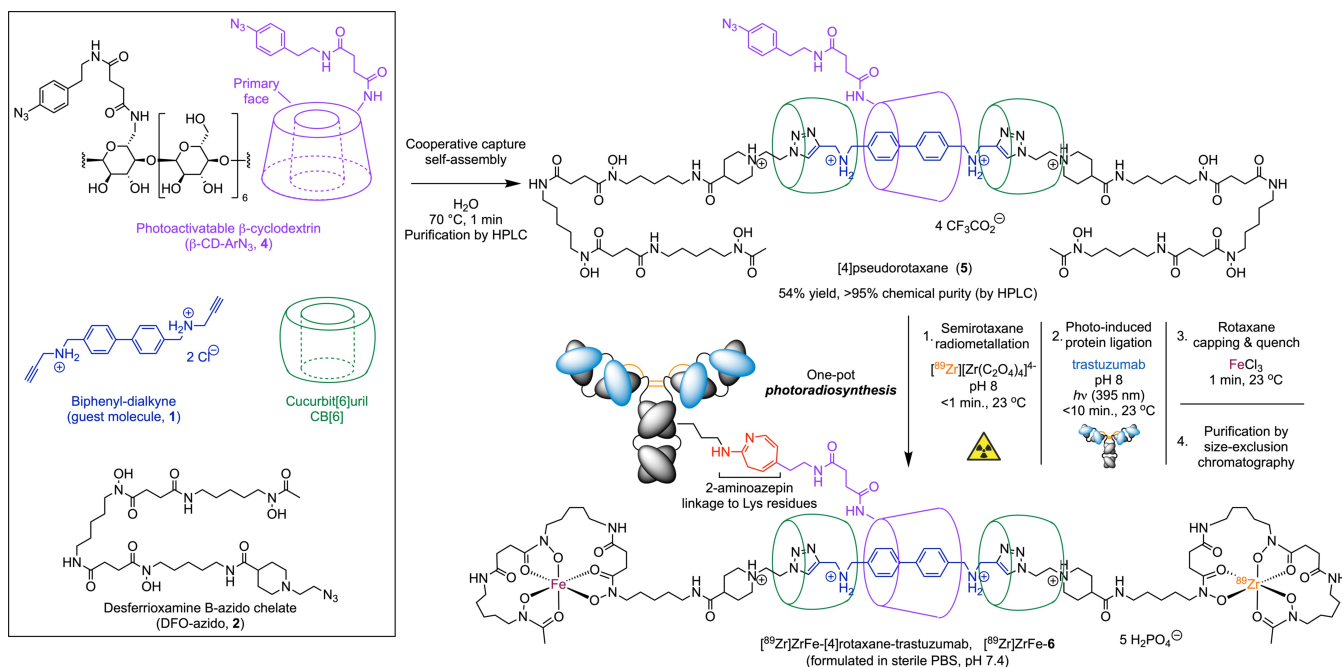
Scheme 2. Synthesis of [89]Zr-radiolabelled rotaxane-trastuzumab showing the components used in the synthesis of the photoactivatable [4]pseudorotaxane **5** and the bimetallic [[89]Zr]ZrFe-[4]rotaxane which is conjugated to the monoclonal antibody trastuzumab by using light-induced protein ligation.[42]
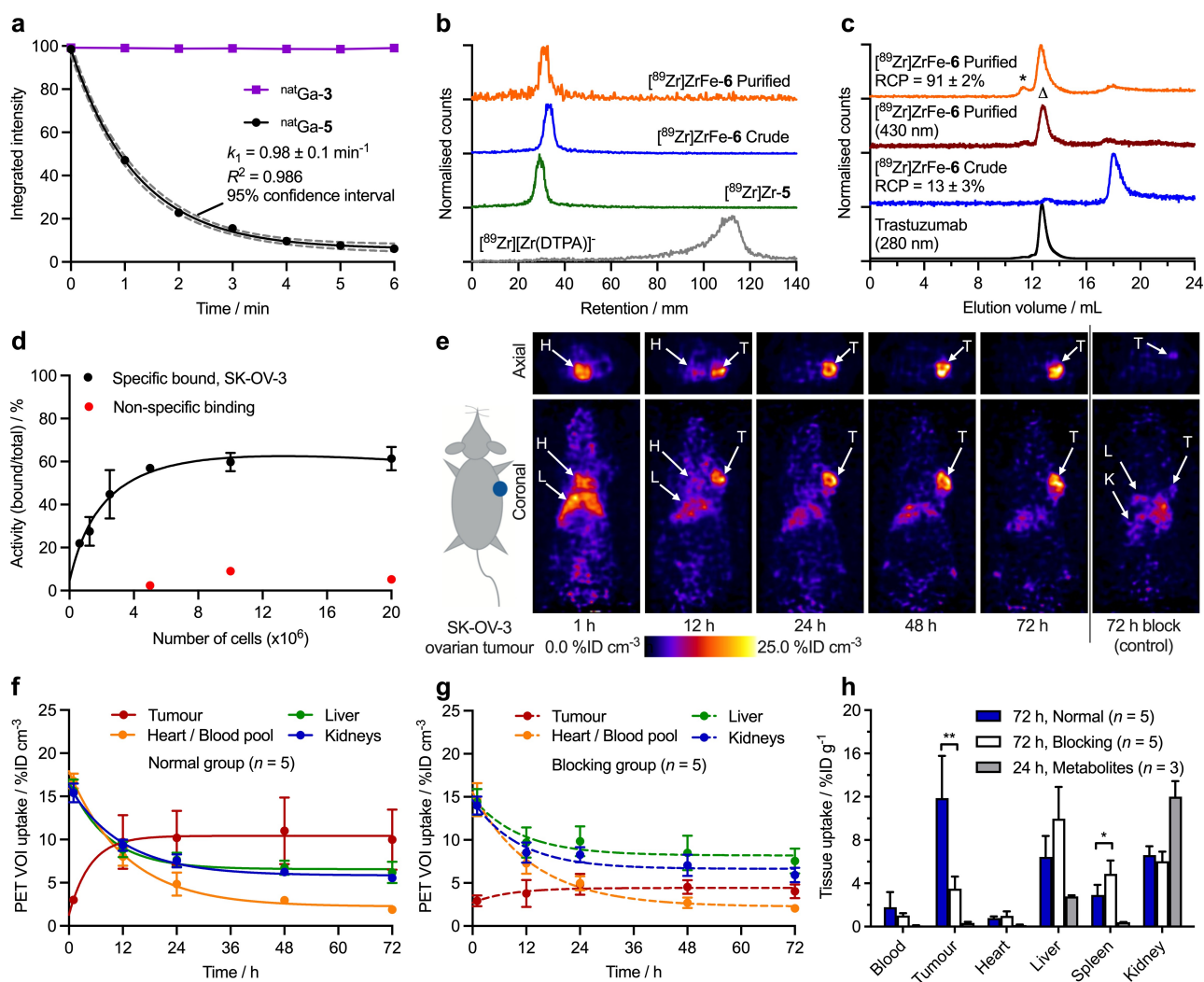
Figure 3. Characterisation of ^{89}Zr-radiolabelled rotaxane-trastuzumab for targeted PET imaging of HER2/*neu* expression in vivo. a) Plot showing the relative photochemical stability versus time (measured by HPLC peak integration) of metallo[4]rotaxanes ^{nat}Ga-**3** (purple) and ^{nat}Ga-**5** (black) under irradiation (395 nm). b) Radio-TLC chromatograms showing the intermediate metallo[4]rotaxane [^{89}Zr]Zr-**5** (green), and the crude (blue) and purified (orange) samples of [^{89}Zr]ZrFe-**6**. c) Analytical SEC-HPLC chromatograms showing the elution profile of trastuzumab (280 nm, black), and the crude (blue) and purified (detection method: radioactivity = orange, 430 nm = red) samples of [^{89}Zr]ZrFe-**6**. Note: "Δ" denotes the monomeric mAb; "*" corresponds to an aggregated protein fraction. d) Cellular saturation binding curves (Lindmo-type assay)[45] showing the specific binding of [^{89}Zr]ZrFe-**6** to SK-OV-3 cells in vitro. e) Representative PET images showing the distribution of [^{89}Zr]ZrFe-**6** (0.161–0.175 MBq, 36–40 μg of protein, molar activity A_m = 0.604–0.671 MBq nmol^{-1}) between 1–72 h post-intravenous administration in a female athymic nude mouse bearing a subcutaneous SK-OV-3 tumour. Control images show the modulation of tumour uptake in a blocking animal (0.170–0.175 MBq, 1190–1230 μg of protein, A_m = 0.020–0.021 MBq nmol^{-1}). Note: T = tumour, H = heart, L = liver, K = kidney. f) Time-activity curves obtained from quantitative volume-of-interest analysis from the normal (n = 5), and g) the blocking (n = 5) group of animals illustrating the tumour specificity of [^{89}Zr]ZrFe-**6**. h) Bar chart showing the biodistribution of [^{89}Zr]ZrFe-**6** in selected tissues from the normal (blue) and blocking (white) groups. Grey bars show the biodistribution of the control sample assigned to [^{89}Zr]ZrFe-[4]rotaxane-2-hydroxyazepin.[46]

sion occurred to give the intermediate [4]semirotaxane [^{89}Zr]Zr-**5** (Figure 3b, green), and that no "free" ^{89}Zr^{4+} ions were present in either the crude (blue) or purified (orange) samples of [^{89}Zr]ZrFe-**6**. Analytical SEC-HPLC analysis with both electronic absorption and radioactivity detection confirmed that the ^{89}Zr-activity eluted at the same point (peak ≈12.7 mL; indicated by "Δ" Figure 3c, orange) as the trastuzumab protein peak measured at 280 nm (black). Comparison of chromatograms from the crude versus purified samples of [^{89}Zr]ZrFe-**6** confirmed the efficiency of the single-step purification process. The FeDFO complex

shows a strong absorption band centred at 430 nm, and the chromatogram of the purified sample, monitored at this wavelength (Figure 3c, red), confirmed that the radio-labelled rotaxane was capped by both ^{89}Zr^{4+} and Fe^{3+} ions. As anticipated, control reactions performed in the dark showed that [^{89}Zr]Zr-**5** is formed but no binding of the ^{89}Zr-radioactivity to the protein fraction occurs in the absence of light (Figure S81).

Before testing [^{89}Zr]ZrFe-**6** in animals, cellular satura-tion binding experiments[45] were performed to estimate the immunoreactive fraction by using SK-OV-3 human ovarian

cancer cells in vitro. Binding experiments confirmed that [^{89}Zr]ZrFe-**6** was biologically active and displayed specific binding to HER2/*neu* with a measured immunoreactive fraction of $61 \pm 5\%$ ($n=3$; Figure 3d, and Figure S82).

The radiosynthesis of [^{89}Zr]ZrFe-**6** was scaled-up to obtain sufficient activity for small-animal PET imaging and biodistribution studies in female athymic nude mice bearing subcutaneous SK-OV-3 xenografts on the right flank. Animals ($n=5$ mice/group) were randomly assigned to two groups which received [^{89}Zr]ZrFe-**6** (in sterile PBS, pH 7.4) as either a normal higher molar activity dose ($A_m = 0.604$–0.671 MBq nmol^{-1} of protein) or a blocking dose that contained the same amount of activity but an increased mass of protein ($A_m = 0.020$–0.021 MBq nmol^{-1}). The blocking group is a standard control used to demonstrate the specific binding of [^{89}Zr]ZrFe-**6** in vivo, through modulation of the tumour uptake by saturating the available HER2/*neu* receptors. Tomographic PET image data (Figure 3e) as well as maximum intensity projects (MIPs; Figure S83, S84) confirmed the high tumour uptake and specificity of [^{89}Zr]ZrFe-**6** for detecting HER2/*neu*-expression in SK-OV-3 xenografts. Quantitative volume-of-interest (VOI) analysis of the PET data versus time produced time-activity curves (TACs) for the normal and blocking groups (Figures 3f and g, Figure S85 and Table S2). PET data revealed that tumour-specific uptake of [^{89}Zr]ZrFe-**6** in the normal group reached $9.99 \pm 3.48\%$ID cm^{-3} (percentage injected dose per cubic centimetre) at 72 h post-radiotracer injection. In comparison, tumour uptake of [^{89}Zr]ZrFe-**6** was reduced by $\approx 60\%$ in the blocking group ($4.02 \pm 0.81\%$ID cm^{-3}, P-value $= 0.0070$). TAC data showed that, excluding the tumour, no difference was observed in the pharmacokinetic profile of [^{89}Zr]ZrFe-**6** in the two groups. Clearance of [^{89}Zr]ZrFe-**6** from the blood pool had a measured half-life of 8.75 ± 1.64 h for the normal group and 9.34 ± 2.67 h for the blocking group.

After the final imaging time point, animals were euthanised and biodistribution analysis was performed to quantify the radiotracer distribution across 15 tissues (Figure 3h, Figure S86 and Table S3). The biodistribution data corroborated the accuracy of the PET images, revealing a tumour-associated accumulation of $11.88 \pm 3.90\%$ID g^{-1} (percentage injected dose per gram) in the normal group and a reduction of $>70\%$ in the blocking group ($3.51 \pm 1.12\%$ID g^{-1}, P-value $= 0.0068$).

As an additional control, PET images and biodistribution data were recorded for [^{89}Zr]ZrFe-[4]rotaxane-2-hydroxyazepin, which is the main small-molecule byproduct formed by hydrolysis of the ketenimine[48] intermediate during the photoradiosynthesis ("metabolite" sample, Figure S87, S88 and Table S4).[46] Imaging data confirmed that [^{89}Zr]ZrFe-[4]rotaxane-2-hydroxyazepin was rapidly extracted from the blood pool and eliminated mainly via renal excretion. Measurements of the effective half-life ($t_{1/2}$(eff) / h) for whole-body excretion were also performed (Figure S89) revealing no difference in the elimination rates of [^{89}Zr]ZrFe-**6** between the normal (8.85 ± 0.72 h [$n=5$]) and blocking groups (8.19 ± 0.77 h [$n=5$]). However, [^{89}Zr]ZrFe-[4]rotaxane-2-hydroxyazepin was eliminated rapidly through

the kidneys with $t_{1/2}$(eff) $= 0.53 \pm 0.14$ h ($n=3$). In comparison with [^{89}Zr]ZrDFO-azepin-trastuzumab, which previously displayed $t_{1/2}$(eff) $= 45.7 \pm 7.7$ h in the same mouse model,[44] our rotaxane-based radiotracer [^{89}Zr]ZrFe-**6** showed an improved elimination of the metabolites, reduced bone uptake ($0.86 \pm 0.32\%$ID g^{-1} versus $9.86 \pm 2.29\%$ID g^{-1}), and a more favourable whole-body dosimetry profile. Collectively, the radiochemical data, cellular studies and in vivo experiments demonstrate that supramolecular chemistry is a viable route for developing cancer-targeted radiotracers with tailored pharmacokinetic profiles.

Synthetic flexibility to control the stoichiometry, the spatial arrangement, and the nature of the various components of the rotaxane is crucial in the development of molecular imaging probes (Figure 4a, Schemes S5–S8, Figure S90–S165, and Tables S5–S8). We synthesised three different [4]pseudorotaxanes (compounds **8**, **11**, and **13**) and their ^{nat}Ga or radioactive ^{68}Ga counterparts. The successful cooperative capture synthesis and radiolabelling of $^{nat/68}$Ga-**8** (also $^{nat/68}$Ga-**11** and $^{nat/68}$Ga-**13**) was confirmed by radio-TLC and analytical HPLC methods (Figures 4b and c, respectively). Metallo[4]rotaxane $^{nat/68}$Ga-**8**, features the same axle as **3** and **5**, but the β-CD macrocycle was functionalised with a small-molecule urea-linked Glu–NH–CO–NH–Lys peptidic-inhibitor that binds to prostate-specific membrane antigen (PSMA), a well-established and clinically validated biomarker of aggressive prostate cancer (PCa).[49]

In metallo[4]rotaxane $^{nat/68}$Ga-**11**, the position of the PSMA inhibitor was swapped to the axle termini and an alternative β-CD functionalised with an *aza*-macrocyclic chelate (NODAGA) was synthesised (compound **9**). Metallo[4]rotaxane $^{nat/68}$Ga-**13** provides another example where a different PSMA-binding ligand, the bioactive component of the approved radiopharmaceutical ^{177}Lu-PSMA-617 (Pluvicto^{TM}, Novartis), was installed as a symmetric axle capping group.

Radiotracers [^{68}Ga]Ga-**8**, [^{68}Ga]Ga-**11**, and [^{68}Ga]Ga-**13** were obtained in high decay-corrected RCYs ($>99\%$) and high RCPs ($>98\%$, measured by radioactive analytical HPLC). Binding and internalisation assays using LNCaP (PSMA-positive), and PC-3 (PSMA-negative) prostate cancer cells were performed to investigate if these rotaxane-based radiotracers could detect PSMA expression (Figure 4d, blue and purple bars, respectively). The clinical grade radiotracer, [^{68}Ga]GaPSMA-11 was used as a positive control and the non-targeted rotaxane radiotracer [^{68}Ga]Ga-**3** was used as a negative control. For the LNCaP cell line, additional assays using 0.1% NaN$_3$ (Figure 4d, white bars) which prevents surface receptor internalisation, and blocking studies using a large excess of the Glu–NH–CO–NH–Lys compound **28** (Figure 4d, grey bars, and Scheme S5) were performed. [^{68}Ga]GaPSMA-11 shows the expected biochemical profile of a viable PSMA-targeted radiotracer whereby cellular associated activity was $3.85 \pm 0.64\%$ ($n=3$) in untreated LNCaP cells and showed a statistically significant difference compared with the NaN$_3$-treated sample ($1.81 \pm 0.87\%$; $n=3$, P-value < 0.05), the ligand-blocked sample ($0.22 \pm 0.06\%$; $n=3$, P-value < 0.01), and the PC-3 cellular control ($0.05 \pm 0.01\%$; $n=3$, P-value $<$
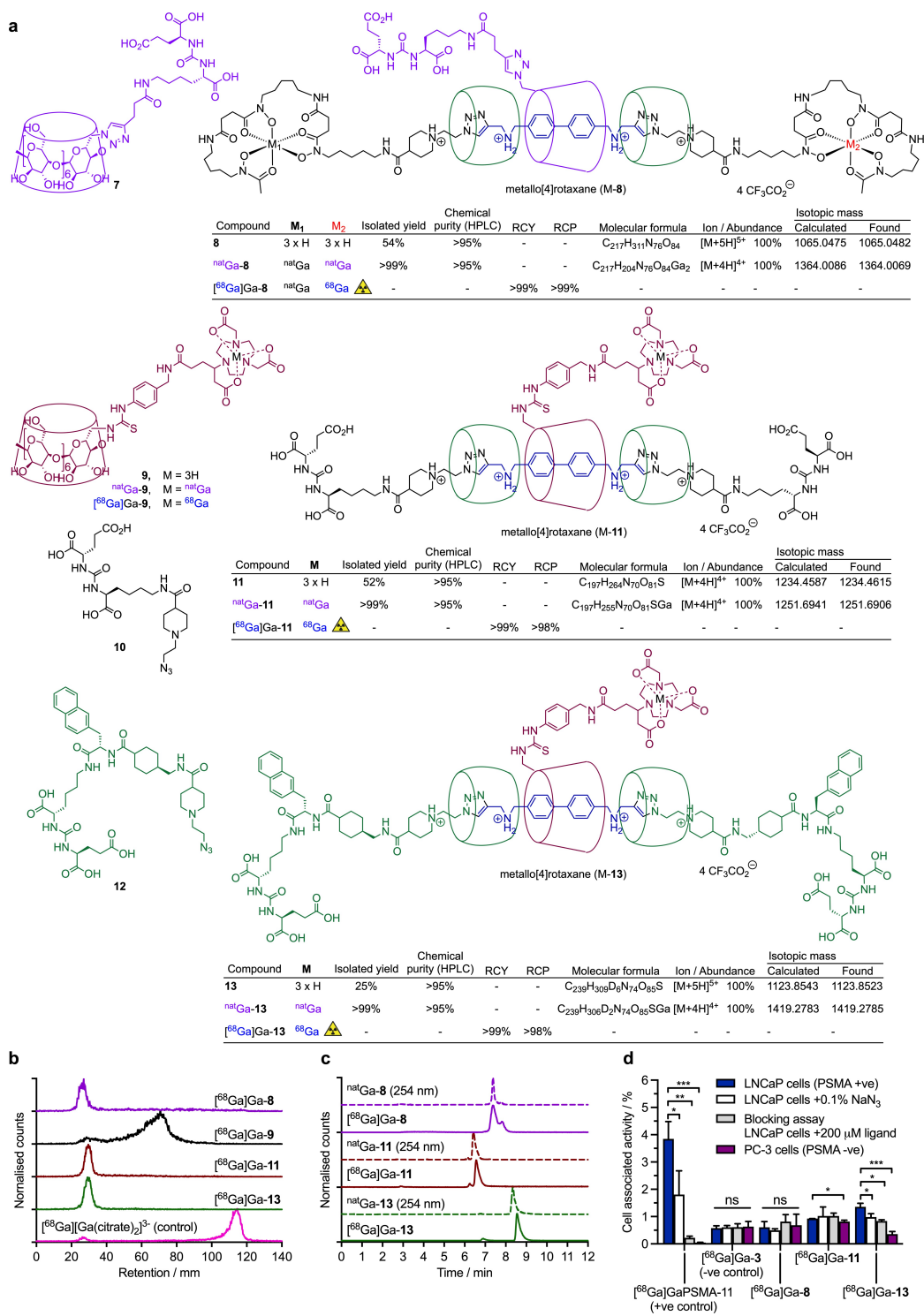
Figure 4. Rotaxane-peptide constructs with versatile composition. a) Chemical structures of the key reagents, the [4]pseudorotaxanes **8**, **11**, and **13**, and their ^{nat}Ga and ^{68}Ga-radiolabelled metallo[4]rotaxane equivalents. b) Radio-TLC chromatograms showing the successful radiosynthesis of [^{68}Ga]Ga-**8** (purple), [^{68}Ga]Ga-**9** (black; the ^{68}Ga-labelled complex of the NODAGA-functionalised β-CD), [^{68}Ga]Ga-**11** (red), and [^{68}Ga]Ga-**13** (green). c) Analytical reverse-phase C18 HPLC chromatograms showing the elution profile of the ^{nat}Ga^{3+} complexes (dash lines) and the radiolabelled ^{68}Ga^{3+} metallo[4]rotaxanes (solid lines) for $^{nat/68}$Ga-**8** (purple), $^{nat/68}$Ga-**11** (red), and $^{nat/68}$Ga-**13** (green). Note: chromatograms of the non-radiolabelled species were measured by electronic absorption at 254 nm. d) Bar chart showing the percentage of cellular bound activity for [^{68}Ga]GaPSMA-11 (positive control), [^{68}Ga]Ga-**3** (negative control), and the test compounds [^{68}Ga]Ga-**8**, [^{68}Ga]Ga-**11**, and [^{68}Ga]Ga-**13**. Note: LNCaP cells (PSMA-positive) are the positive model (blue); PC-3 cells (PSMA-negative) were used as a negative control line (purple) to measure non-specific binding. The addition of 0.1 % NaN$_3$ to the LNCaP binding assay (white) prevents PSMA receptor internalisation. The blocking assay (grey) provides a measure of binding specificity and involved pre-incubation of the LNCaP cells with an excess of the free Glu−NH−CO−NH−Lys inhibitor **28** (200 μM).

0.001). The control [68Ga]Ga-**3**, and metallo[4]rotaxanes [68Ga]Ga-**8** and [68Ga]Ga-**11** showed no specific interaction with PSMA, suggesting that the Glu–NH–CO–NH–Lys ligand was not able to access the catalytic protein binding pocket. In contrast, [68Ga]Ga-**13** displayed the correct biochemical behaviour with the same binding trends observed for [68Ga]GaPSMA-11. The total cellular bound activity of [68Ga]Ga-**13** was approximately 4-fold lower than [68Ga]GaPSMA-11, which precluded further animal studies based on ethical considerations, but this was anticipated since the clinical-grade radiotracer emerged after extensive structure–activity optimisation.[49] Nevertheless, these data provide an encouraging precedent that rotaxane radiotracers featuring drugs or peptides can be developed for applications in molecular imaging.

Next, we reduced the number of components and synthesised both a metallo[3]semirotaxane, and a fluorescein-capped metallo[3]rotaxane for dual-modality PET/optical imaging (Figure 5, Schemes S9–S11, Figure S166–S245, and Tables S7–S10).

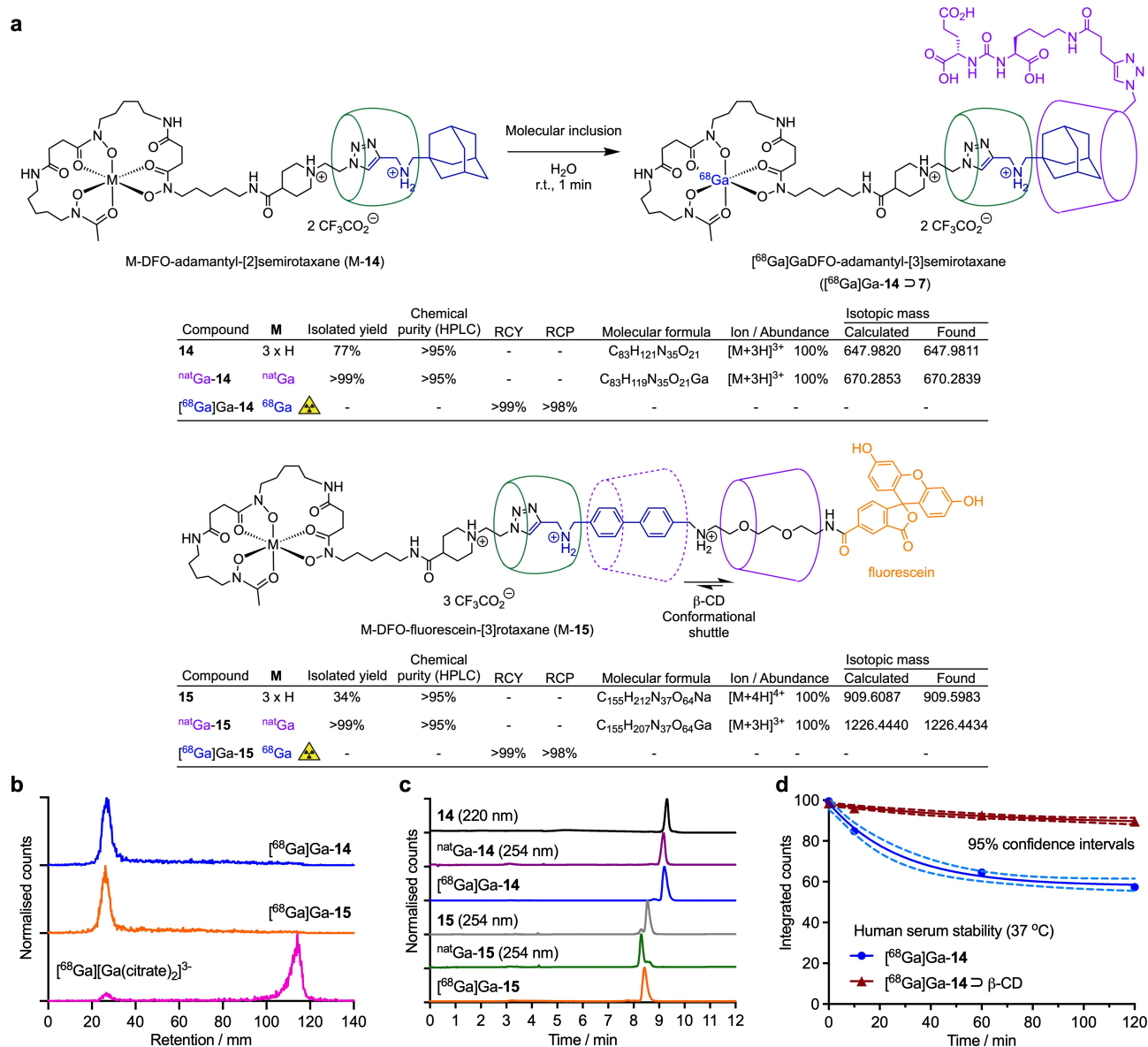Cooperative capture was used to synthesise [2]semirotaxane **14** in 77 % yield. During HPLC purification

a

M-DFO-adamantyl-[2]semirotaxane (M-**14**)

[68Ga]GaDFO-adamantyl-[3]semirotaxane ([68Ga]Ga-**14** ⊃ **7**)

Compound	M	Isolated yield	Chemical purity (HPLC)	RCY	RCP	Molecular formula	Ion / Abundance		Isotopic mass	
									Calculated	Found
14	3 × H	77%	>95%	-	-	$C_{83}H_{121}N_{35}O_{21}$	$[M+3H]^{3+}$	100%	647.9820	647.9811
nat Ga-**14**	nat Ga	>99%	>95%	-	-	$C_{83}H_{119}N_{35}O_{21}Ga$	$[M+3H]^{3+}$	100%	670.2853	670.2839
[68Ga]Ga-**14**	68Ga ⚠️	-	-	>99%	>98%	-	-	-	-	-

M-DFO-fluorescein-[3]rotaxane (M-**15**)

Compound	M	Isolated yield	Chemical purity (HPLC)	RCY	RCP	Molecular formula	Ion / Abundance		Isotopic mass	
									Calculated	Found
15	3 × H	34%	>95%	-	-	$C_{155}H_{212}N_{37}O_{64}Na$	$[M+4H]^{4+}$	100%	909.6087	909.5983
nat Ga-**15**	nat Ga	>99%	>95%	-	-	$C_{155}H_{207}N_{37}O_{64}Ga$	$[M+3H]^{3+}$	100%	1226.4440	1226.4434
[68Ga]Ga-**15**	68Ga ⚠️	-	-	>99%	>98%	-	-	-	-	-

b

c

d

Figure 5. Synthesis and characterisation of a metallo[3]semirotaxane, and an asymmetric metallo[3]rotaxane for dual modality imaging. a) Reaction scheme and chemical structures of the asymmetric [4]semirotaxanes **14** and **15**, and M-**14**⊃**7** (M = 3H atoms, or nat/68Ga), and the fluorescein-conjugated metallo[3]rotaxanes nat/68Ga-**15**. b) Radio-TLC chromatograms showing the radiosynthesis of metallo[2]rotaxane [68Ga]Ga-**14** (blue), and metallo[3]rotaxane [68Ga]Ga-**15** (orange). c) Analytical reverse-phase C18 HPLC chromatograms showing the elution profile of **14** (black, 220 nm), **15** (grey, 254 nm), the corresponding nat Ga3+ complexes nat Ga-**14**, (purple), and nat Ga-**15**, (green), and the radiolabelled 68Ga3+ species [68Ga]Ga-**14**, (blue), and [68Ga]Ga-**15**, (orange). d) Plot showing the relative stability versus time of [68Ga]Ga-**14** (blue) and [68Ga]Ga-**14**⊃β-CD (purple) during incubation in human serum (37 °C, pH 7.4).

under acidic conditions, β-CD dissociated. Then **14** was metallated to give the metallo[2]rotaxanes natGa-**14** or radiolabelled [68Ga]Ga-**14** (Figure 5, and Schemes S9, S10, Figure S166–S193, Tables S7–S9). Characterisation by radio-TLC, and analytical HPLC, confirmed the successful radiosynthesis of [68Ga]Ga-**14** (Figures 5b and **5c**). Stability studies in water confirmed that both **14** and natGa-**14** remained intact for at least 96 h (Figure S189). Compound **14** features a bulky, lipophilic adamantyl group, which under neutral conditions, forms a tightly bound molecular inclusion complex with β-CD. ¹H NMR titration experiments with the intermediate adamantyl salt **37** and β-CD gave an average binding constant for the **37**⊃β-CD inclusion complex of $K_a = 19\,883 \pm 4429$ M⁻¹ (Figure S172–S178, and Table S7). Molecular inclusion reactions between **14** or nat/68Ga-**14**, and β-CD in water, produced the [3]semirotaxane **14**⊃β-CD, and the metallo[3]semirotaxanes nat/68Ga-**14**⊃β-CD (Figure S190–S193). Stability studies in human serum indicated that [68Ga]Ga-**14** degraded but [68Ga]Ga-**14**⊃β-CD remained stable (Figure 5d, Figure S194 and Table S9). We also prepared molecular inclusion complexes with the PSMA-targeted β-CD-derivative **7** to give the [3]semirotaxanes **14**⊃**7**, and nat/68Ga-**14**⊃**7** (Figure S195–S198). Cellular binding studies were performed with the non-targeted [68Ga]Ga-**14**⊃β-CD and the PSMA-targeted [68Ga]Ga-**14**⊃**7** species (Figure S199). The absolute cellular uptake was low, which excluded their use in vivo based on ethical considerations, but encouragingly, the PSMA-targeted [68Ga]Ga-**14**⊃**7** displayed the correct biochemical behaviour with an ≈75% decrease in binding between the LNCaP (PSMA-positive) and the PC-3 (PSMA-negative) cells.

The [3]semirotaxane **15** was synthesised in 34% isolated yield. Metallation gave the corresponding metallo-[3]rotaxanes natGa-**15** and [68Ga]Ga-**15**. Compound **15** features an asymmetric axle capped by a (radio)metal ion complex and a fluorescein derivative for potential applications in dual-modality PET/optical fluorescence imaging (Figure 5, Scheme S11, Figure S200–S245, and Table S10). Radio-TLC and analytical HPLC confirmed the successful radiosynthesis with high chemical purity (>95%) and RCP (>98%) of [68Ga]Ga-**15** (Figures 5b and **5c**). ¹H NMR titrations indicated that the biphenyl-polyethylene glycol (PEG) intermediate **42**, and the biphenyl-fluorescein compound **43**, form 1:1 inclusion complexes with β-CD, where the average binding constants were $K_a(\textbf{42} \supset \beta\text{-CD}) = 2340 \pm 577$ M⁻¹ and $K_a(\textbf{43} \supset \beta\text{-CD}) = 167 \pm 70$ M⁻¹ (Figure S223–S233, and Table S10). In contrast to the 1-minute reaction times required for the synthesis of symmetrical [4]pseudorotaxanes **3** and **5**, the synthesis of **15** required heating for 12 h. Conformational equilibrium where the β-CD macrocycle resides primarily over the PEG₂ chain would reduce the interaction between the CB[6] and β-CD macrocycles, decreasing the rate of the cooperative capture process.[34–38]

Conclusion

Experiments demonstrate the synthetic flexibility of using self-assembly methods to create multifunctional, asymmetric rotaxanes for applications in molecular imaging. Tumour-specific uptake of a supramolecular rotaxane-based radiolabelled mAb was observed in vivo where PET imaging and biodistribution analysis were used to study the pharmacokinetics of [89Zr]ZrFe-[4]rotaxane-trastuzumab. Synthetic variations of the rotaxane architecture were also explored, demonstrating that the system composition can be easily tuned. Collectively, these data provide compelling evidence that rotaxane-based supramolecular chemistry is a versatile platform for designing molecular imaging probes that target biomarkers of disease.

Acknowledgements

Conflict of Interest

The authors declare no conflict of interest.

Data Availability Statement

The data that support the findings of this study are available from the corresponding author upon reasonable request.

Keywords: Molecular Imaging · Molecularly Interlocked Molecules · Radiochemistry · Rotaxanes · Supramolecular Chemistry

[1] C. J. Bruns, J. F. Stoddart, *The Nature of the Mechanical Bond*, Wiley, Hoboken, **2016**.
[2] E. A. Neal, S. M. Goldup, *Chem. Commun.* **2014**, *50*, 5128–5142.
[3] A. Livoreil, C. Dietrich-Buchecker, J. Sauvage, *J. Am. Chem. Soc.* **1994**, *116*, 9399–9400.
[4] R. A. Bissell, E. Cordova, A. E. Kaifer, J. F. Stoddart, *Nature* **1994**, *369*, 133–137.
[5] S. Erbas-Cakmak, D. A. Leigh, C. T. McTernan, A. L. Nussbaumer, *Chem. Rev.* **2015**, *115*, 10081–10206.
[6] S. P. Fletcher, F. Dumur, M. M. Pollard, B. L. Feringa, *Science* **2005**, *310*, 80–83.
[7] S. F. M. Van Dongen, S. Cantekin, J. A. A. W. Elemans, A. E. Rowan, R. J. M. Nolte, *Chem. Soc. Rev.* **2014**, *43*, 99–122.

[8] Y. Luo, C. P. Collier, J. O. Jeppesen, K. A. Nielsen, E. DeIonno, G. Ho, J. Perkins, H. R. Tseng, T. Yamamoto, J. F. Stoddart, J. R. Heath, *ChemPhysChem* **2002**, *3*, 519–525.

[9] S. Angelos, Y. Yang, K. Patel, J. F. Stoddart, J. I. Zink, *Angew. Chem. Int. Ed.* **2008**, *47*, 2222–2226; *Angew. Chem.* **2008**, *120*, 2254–2258.

[10] M. Galli, J. E. M. Lewis, S. M. Goldup, *Angew. Chem. Int. Ed.* **2015**, *54*, 13545–13549; *Angew. Chem.* **2015**, *127*, 13749–13753.

[11] A. W. Heard, S. M. Goldup, *Chem* **2020**, *6*, 994–1006.

[12] N. Pairault, R. Barat, I. Tranoy-Opalinski, B. Renoux, M. Thomas, S. Papot, *C. R. Chim.* **2016**, *19*, 103–112.

[13] A. Casini, B. Woods, M. Wenzel, *Inorg. Chem.* **2017**, *56*, 14715–14729.

[14] X. Wang, D. B. Smithrud, *Bioorg. Med. Chem. Lett.* **2011**, *21*, 6880–6883.

[15] D. B. Smithrud, L. Powers, J. Lunn, S. Abernathy, M. Peschka, S. mei Ho, P. Tarapore, *ACS Med. Chem. Lett.* **2017**, *8*, 163–167.

[16] M. Sojka, M. Fojtu, J. Fialova, M. Masarik, M. Necas, R. Marek, *Inorg. Chem.* **2019**, *58*, 10861–10870.

[17] M. J. Webber, R. Langer, *Chem. Soc. Rev.* **2017**, *46*, 6600–6620.

[18] R. Barat, T. Legigan, I. Tranoy-Opalinski, B. Renoux, E. Péraudeau, J. Clarhaut, P. Poinot, A. E. Fernandes, V. Aucagne, D. A. Leigh, S. Papot, *Chem. Sci.* **2015**, *6*, 2608–2613.

[19] A. Schmidt, V. Molano, M. Hollering, A. Pöthig, A. Casini, F. E. Kühn, *Chem. Eur. J.* **2016**, *22*, 2253–2256.

[20] M. J. Hannon, *Chem. Soc. Rev.* **2007**, *36*, 280–295.

[21] A. Fernandes, A. Viterisi, F. Coutrot, S. Potok, D. A. Leigh, V. Aucagne, S. Papot, *Angew. Chem. Int. Ed.* **2009**, *48*, 6443–6447; *Angew. Chem.* **2009**, *121*, 6565–6569.

[22] A. Fernandes, A. Viterisi, V. Aucagne, D. A. Leigh, S. Papot, *Chem. Commun.* **2012**, *48*, 2083–2085.

[23] B. P. Burke, W. Grantham, M. J. Burke, G. S. Nichol, D. Roberts, I. Renard, R. Hargreaves, C. Cawthorne, S. J. Archibald, P. J. Lusby, *J. Am. Chem. Soc.* **2018**, *140*, 16877–16881.

[24] B. Woods, R. D. M. Silva, C. Schmidt, D. Wragg, M. Cavaco, V. Neves, V. F. C. Ferreira, L. Gano, T. S. Morais, F. Mendes, J. D. G. Correia, A. Casini, *Bioconjugate Chem.* **2021**, *32*, 1399–1408.

[25] E. Arunkumar, N. Fu, B. D. Smith, *Chem. Eur. J.* **2006**, *12*, 4684–4690.

[26] J. J. Gassensmith, J. M. Baumes, B. D. Smith, *Chem. Commun.* **2009**, 6329–6338.

[27] C. Zhai, C. L. Schreiber, S. Padilla-coley, A. G. Oliver, B. D. Smith, *Angew. Chem. Int. Ed.* **2020**, *59*, 23740–23747; *Angew. Chem.* **2020**, *132*, 23948–23955.

[28] J. W. Fredy, J. Scelle, A. Guenet, E. Morel, S. Adam De Beaumais, M. Ménand, V. Marvaud, C. S. Bonnet, E. Tõth, M. Sollogoub, G. Vives, B. Hasenknopf, *Chem. Eur. J.* **2014**, *20*, 10915–10920.

[29] J. W. Fredy, J. Scelle, G. Ramniceanu, B. T. Doan, C. S. Bonnet, É. Tóth, M. Ménand, M. Sollogoub, G. Vives, B. Hasenknopf, *Org. Lett.* **2017**, *19*, 1136–1139.

[30] S. Hou, J. S. Choi, M. A. Garcia, Y. Xing, K. J. Chen, Y. M. Chen, Z. K. Jiang, T. Ro, L. Wu, D. B. Stout, J. S. Tomlinson, H. Wang, K. Chen, H. R. Tseng, W. Y. Lin, *ACS Nano* **2016**, *10*, 1417–1424.

[31] H. Ge, P. J. Riss, V. Mirabello, D. G. Calatayud, S. E. Flower, R. L. Arrowsmith, T. D. Fryer, Y. Hong, S. Sawiak, R. M. J. Jacobs, S. W. Botchway, R. M. Tyrrell, T. D. James, J. S. Fossey, J. R. Dilworth, F. I. Aigbirhio, S. I. Pascu, *Chem* **2017**, *3*, 437–460.

[32] G. V. Oshovsky, D. N. Reinhoudt, W. Verboom, *Angew. Chem. Int. Ed.* **2007**, *46*, 2366–2393; *Angew. Chem.* **2007**, *119*, 2418–2445.

[33] C. J. Bruns, H. Liu, M. B. Francis, *J. Am. Chem. Soc.* **2016**, *138*, 15307–15310.

[34] C. Ke, R. A. Smaldone, T. Kikuchi, H. Li, A. P. Davis, J. F. Stoddart, *Angew. Chem. Int. Ed.* **2013**, *52*, 381–387; *Angew. Chem.* **2013**, *125*, 399–405.

[35] X. Hou, C. Ke, C. Cheng, N. Song, A. K. Blackburn, A. A. Sarjeant, Y. Y. Botros, Y.-W. Yang, J. F. Stoddart, *Chem. Commun.* **2014**, *50*, 6196–6199.

[36] X. Hou, C. Ke, J. Fraser Stoddart, *Chem. Soc. Rev.* **2016**, *45*, 3766–3780.

[37] W. L. Mock, N. Y. Shih, *J. Org. Chem.* **1983**, *48*, 3618–3619.

[38] W. L. Mock, T. A. Irra, J. P. Wepsiec, M. Adhya, *J. Org. Chem.* **1989**, *54*, 5302–5308.

[39] D. Tuncel, J. H. G. Steinke, *Chem. Commun.* **1999**, 1509–1510.

[40] J. A. Finbloom, K. Han, C. C. Slack, A. L. Furst, M. B. Francis, *J. Am. Chem. Soc.* **2017**, *139*, 9691–9697.

[41] A. Guillou, D. F. Earley, M. Patra, J. P. Holland, *Nat. Protoc.* **2020**, *15*, 3579–3594.

[42] D. F. Earley, A. Guillou, S. Klingler, R. Fay, M. Gut, F. d'Orchymont, S. Behmaneshfar, L. Reichert, J. P. Holland, *JACS Au* **2022**, *2*, 646–664.

[43] M. Patra, L. S. Eichenberger, G. Fischer, J. P. Holland, *Angew. Chem. Int. Ed.* **2019**, *58*, 1928–1933; *Angew. Chem.* **2019**, *131*, 1946–1951.

[44] M. Patra, S. Klingler, L. S. Eichenberger, J. P. Holland, *iScience* **2019**, *13*, 416–431.

[45] S. Konishi, K. Hamacher, S. Vallabhajosula, P. Kothari, D. Bastidas, N. Bander, S. Goldsmith, *Cancer Biother. Radiopharm.* **2004**, *19*, 706–15.

[46] A. Guillou, D. F. Earley, S. Klingler, E. Nisli, L. J. Nüesch, R. Fay, J. P. Holland, *Bioconjugate Chem.* **2021**, *32*, 1263–1275.

[47] J. P. Holland, *Inorg. Chem.* **2020**, *59*, 2070–2082.

[48] N. P. Gritsan, M. S. Platz, *Chem. Rev.* **2006**, *106*, 3844–3867.

[49] M. Eder, M. Schäfer, U. Bauder-Wüst, W. E. Hull, C. Wängler, W. Mier, U. Haberkorn, M. Eisenhut, *Bioconjugate Chem.* **2012**, *23*, 688–697.